

DESIGN AND CHARACTERIZATION OF A CUSTOM ASPHERIC LENS
SYSTEM FOR SINGLE ATOM IMAGING

by

MATTHEW BRIEL

A THESIS

Presented to the Department of Physics
and the Graduate School of the University of Oregon
in partial fulfillment of the requirements
for the degree of
Master of Science

June 2012

THESIS APPROVAL PAGE

Student: Matthew Briel

Title: Design and Characterization of a Custom Aspheric Lens System for Single Atom Imaging

This thesis has been accepted and approved in partial fulfillment of the requirements for the Master of Science degree in the Department of Physics by:

Dr. Daniel Steck	Chair
Dr. Stephen Gergory	Member
Dr. Steven van Enk	Member

and

Kimberly Andrews Espy	Vice President for Research & Innovation/ Dean of the Graduate School
-----------------------	--

Original approval signatures are on file with the University of Oregon Graduate School.

Degree awarded June 2012

© 2012 Matthew Briel

THESIS ABSTRACT

Matthew Briel

Master of Science

Department of Physics

June 2012

Title: Design and Characterization of a Custom Aspheric Lens System for Single Atom Imaging

We designed an optical imaging system comprising a pair of custom aspheric lenses for the purpose of making a continuous position measurement of a single rubidium atom in a dipole trap. The lens profiles were determined with optimization and ray-tracing programs written in Fortran. The lenses were produced by Optimax Systems and found to perform as predicted, imaging a point source to a minimal spot size along a wide range of emitter positions.

CURRICULUM VITAE

NAME OF AUTHOR: Matthew Briel

GRADUATE AND UNDERGRADUATE SCHOOLS ATTENDED:

Miami University, Oxford, Ohio
University of Oregon, Eugene, Oregon

DEGREES AWARDED:

Bachelor of Science in Physics, 2009, Miami University
Master of Science in Physics, 2012, University of Oregon

AREAS OF SPECIAL INTEREST:

Quantum Optics, Atom Trapping

PROFESSIONAL EXPERIENCE:

Teaching Assistant, University of Oregon, Eugene, 2009-2012

PUBLICATIONS:

Souther, N., Wagner, R., Harnish, P., Briel, M., and Bali, S. (2010). Measurements of light shifts in cold atoms using raman pump-probe spectroscopy. *Laser Physics Letters*, 7:321–327.

TABLE OF CONTENTS

Chapter	Page
I. BACKGROUND	1
II. RAY TRACING	3
Mathematical Background	3
Proof of Concept	5
III. OPTIMIZATION METHODS	11
Gradient-Descent Optimization	11
Nelder-Mead Algorithm	12
Particle-Swarm Optimization	13
Method Comparison	15
IV. LENS DESIGN	19
V. RESULTS	23
VI. CONCLUSIONS	29
APPENDICES	

Chapter	Page
A. SNELL'S LAW	30
B. INDEX OF REFRACTION DATA	32
C. MECHANICAL DRAWINGS	35
D. ASPHERE PROFILE	38
REFERENCES CITED	39

LIST OF FIGURES

Figure	Page
1. Diagram of the square cell where atom trapping occurs.	2
2. Derivation of the Descartes lens.	6
3. The profile of Descartes' perfect lens and an off-the-shelf plano-convex lens. 7	7
4. Recreated from (Wolf, 1948), for use in deriving aspheric surfaces.	8
5. Diagram for the derivation of the "ideal collimating" asphere for our setup.	9
6. Profile of the Wolf Asphere.	10
7. Pseudocode description of the Gradient-Descent method (Zwillinger, 2003).	11
8. Pseudocode description of the Nelder-Mead method (Wright, 1996).	13
9. Two-dimensional example simplexes from the Nelder-Mead method.	14
10. Pseudocode description of the Particle-Swarm Optimization method (Pedersen, 2009).	15
11. The Rosenbrock function.	16
12. A comparison of the performance of three different optimization methods applied to the Rosenbrock function.	17
13. Scale representation of the imaging system.	20
14. Example of different emitter positions (shown as red spots).	20
15. Optimization of the asphere problem.	21
16. Photo of one of the 30mm diameter custom aspheric lens with a penny for comparison.	23
17. Machined parts for holding the second asphere and optical flat, pictured mounted to the Hamamatsu camera.	24
18. Machined parts for mounting the first asphere to the glass cell.	25

Figure	Page
19. Image of an etched ruler taken with the aspheres. Measurements on top are in millimeters.	26
20. Image of a square reticle showing slight pincushion distortion.	26
21. Image of a single-mode optical fiber at the center of the aspheric imaging system.	26
22. Image of a single-mode optical fiber 0.5 mm away from the center of the aspheric imaging system.	26
23. A series of images as the optical fiber is shifted away from the central axis of the aspheric imaging system.	27
24. Image of a single-mode optical fiber at the center of the plano-convex imaging system.	27
25. Image of a single-mode optical fiber 0.5 mm away from the center of the plano-convex imaging system.	28
26. Image of a single-mode optical fiber approximately 1.5 mm away from the center of the aspheric imaging system.	28
27. Difference in the index of refraction for Spectrosil 2000 and fused silica.	33
28. Mechanical drawing of the asphere collar and mounting peice.	35
29. Mechanical drawing of the asphere mounting parts for the Hamamatsu camera.	36
30. Detail drawings of the glass plate holder and the asphere collar.	37

LIST OF TABLES

Table	Page
1. Suggested values for Nelder-Mead parameters.	14
2. Suggested ranges for Particle-Swarm parameters.	15
3. Generalized number of function calls for each method per iteration. . .	17
4. Total number of function calls necessary to minimize the Rosenbrock function.	18
5. Image size as a function of emitter position for the optimized asphere. .	21
6. Sellmeier constants for Spectrosil 2000 and fused silica.	32
7. Cauchy constants for the index matching materials.	33
8. The index of refraction of all three index matching materials at 780 nm.	34
9. Final values for the parameters of the asphere equation.	38

CHAPTER I

BACKGROUND

Our current research goal is to move from a standard magneto-optical atom trap to a single atom trap. The motivation for this is to study the motion of single atoms moving through a dipole trap. After that we plan to implement a feedback system that determines the atom's position, and then controls the system to actively cool the atom further. To do this we need a robust system for determining a single atom's position within the trap.

A successful imaging system will need to fulfill two important requirements: it must collect as much light as possible, and it should be able to focus light to a point independently of the source's transverse position.

Imaging systems with a large numerical aperture generally deal with effects like spherical aberration by increasing the number of optical elements involved or introducing aspheric elements. However, systems with many optical elements are a challenge to set up and difficult to maintain.

One group (Blinov, 2009) achieved a large numerical aperture imaging system by placing a spherical mirror behind their trapped atoms, allowing the collection of both forward and backward emitted light. The numerical aperture of 0.9 allows for a large collection percentage, though the system performs poorly as atoms move off-axis. Additionally, implementing a system of this type would require breaking the vacuum on our system to place the spherical mirror and the manufacturing of a custom aspheric plate to correct for aberrations introduced by the spherical mirror.

Another group (Alt, 2008) built an imaging system with four stock lenses, optimizing their relative positions and radii of curvature to generate small spot

sizes both on- and off-axis . The main drawback to this system is its small numerical aperture of 0.29. This would not provide a sufficiently large count rate to make imaging a single atom feasible.

Our system is shown in Fig. 1. Atoms are first collected by a magneto-optical trap, and then transferred to a far-off-resonance dipole trap. To maximize light collection from the trapped atom we designed a system in which the first element is in contact with the cell. This would make it possible for a ray leaving the source at nearly a 45° angle to be collected, making the maximum numerical aperture of the system 0.7.

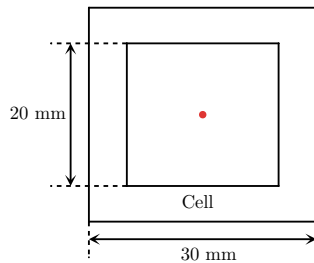


FIGURE 1. Diagram of the square cell where atom trapping occurs.

With recent advances in lens manufacturing technology, building lenses with custom profiles has become affordable. We feel that the best direction then is to have a pair of aspheric lenses with a profile optimized to image a point source back to a point as it moves along a line perpendicular to the axis of the lenses with as little aberration as possible. A pair of custom lenses can satisfy all our requirements and would be simple to implement.

CHAPTER II

RAY TRACING

Ray tracing is the method of simulating an image by tracking rays of light from their point of origin through any obstacle onto an imaging surface, by obeying the laws of geometric optics. As a result, ray tracing will not account for diffractive effects, though it is vastly more computationally efficient than a full wave simulation. The method works in free space and any medium with a homogeneous index of refraction.

The goal here is to write a ray tracing program that will allow us to simulate images generated by different optical systems implemented in our setup. We begin by outlining a general method for tracking a ray as it crosses an optical interface.

Mathematical Background

Consider a ray of light represented as,

$$x(t) = x_0 + \alpha t \tag{2.1}$$

$$y(t) = y_0 + \beta t \tag{2.2}$$

$$z(t) = z_0 + \gamma t, \tag{2.3}$$

parametrized by some variable t , and subject to the constraint $\alpha^2 + \beta^2 + \gamma^2 = 1$.

Then we consider the ray crossing an interface having a surface profile given by some function $f(r)$. While it is not necessary, we will only consider cylindrically symmetric surface profiles.

We construct the radial function $r(t)$ and the vector function $A(\theta, t)$ describing the surface of the interface:

$$r(t) = \sqrt{x(t)^2 + y(t)^2}, \quad (2.4)$$

$$\vec{A} = \vec{A}(\theta, t) = \begin{pmatrix} r(t) \cos \theta \\ r(t) \sin \theta \\ f(r(t)) \end{pmatrix}. \quad (2.5)$$

We find the intersection of the ray and the interface with Newton's method, a standard root-solving technique, applied to the equation $f(r(t)) = z_0 + \gamma t$. Let τ denote the solution time. Then what is left is to determine the angle at which the ray leaves the surface. For this we use a vector implementation as outlined by (Glassner, 1989). This requires defining the unit normal vector to the surface at the intersection point, a standard result from vector calculus,

$$\hat{N} \equiv \frac{\vec{A}_\theta \times \vec{A}_t}{|\vec{A}_\theta \times \vec{A}_t|}, \quad (2.6)$$

where the usual definitions for derivatives apply,

$$\vec{A}_\theta \equiv \frac{\partial \vec{A}}{\partial \theta} = \begin{pmatrix} -r(t) \sin \theta \\ r(t) \cos \theta \\ 0 \end{pmatrix}, \quad \vec{A}_t \equiv \frac{\partial \vec{A}}{\partial t} = \begin{pmatrix} \frac{\partial r(t)}{\partial t} \cos \theta \\ \frac{\partial r(t)}{\partial t} \sin \theta \\ \frac{\partial f(t)}{\partial t} \end{pmatrix}. \quad (2.7)$$

It is trivial from here to construct the unit normal vector to the surface. Snell's law also requires a vector that points from the light source towards its intersection with

the interface, which we may write as

$$\vec{L}(t) = \begin{pmatrix} x(0) - x(\tau) \\ y(0) - y(\tau) \\ z(0) - z(\tau) \end{pmatrix}. \quad (2.8)$$

Before using \vec{L} , it must be normalized in the usual sense. The necessary components of Snell's Law follow as:

$$\cos(\theta_1) = \hat{N} \cdot (-\hat{L}), \quad (2.9)$$

$$\cos(\theta_2) = \sqrt{1 - \left(\frac{n_1}{n_2}\right)^2 (1 - (\cos(\theta_1))^2)}, \quad (2.10)$$

$$\hat{v}_{\text{refract}} = \left(\frac{n_1}{n_2}\right) \hat{L} + \left(\frac{n_1}{n_2} \cos(\theta_1) - \cos(\theta_2)\right) \hat{N}. \quad (2.11)$$

We have found that the ray intersects the surface at $(x(\tau), y(\tau), f(r(\tau)))$, and that $\hat{v}_{\text{refract}} = (\alpha', \beta', \gamma')$, the ray's new direction after crossing the interface. Proof that \hat{v}_{refract} is a unit vector can be found in Appendix A.

Proof of Concept

Descartes Lens

Descartes discovered a form for a lens that would perfectly collimate light from a point source. In Fig. 2. we see two rays passing through a lens with an index of refraction n . To determine what shape would collimate the light from a point source, we equate the optical path length of the two rays:

$$f + ny = \sqrt{(f + y)^2 + r^2}. \quad (2.12)$$

Solving this equation, we find the surface profile of the lens,

$$y(r) = \frac{nf}{(n+1)} + \frac{\sqrt{(n-1)^2 f^2 + (n^2-1)r^2}}{(n^2-1)}, \quad (2.13)$$

a function of the lens' index of refraction n , and its front focal length f . In Fig. 3. we compare the profile of this lens to a stock plano-convex lens from Newport.¹ This is done by matching f and n to the Newport lens' focal length and index of refraction.

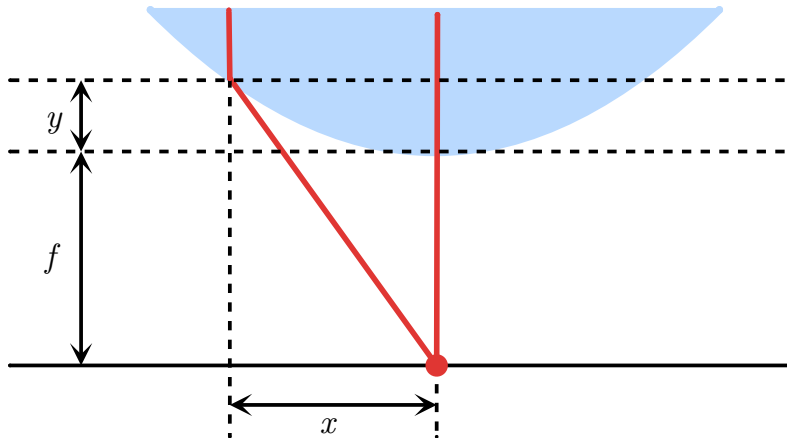


FIGURE 2. Derivation of the Descartes lens.

We use the ray tracing software to image a point source through the Descartes lens, simulating the image. Once we have the coordinates where each ray intersects the image plane we generate a quantity called the image size by calculating the root-mean-square position of every ray. Every calculation uses 10,000 rays distributed according to the linear dipole radiation pattern, with the dipole oriented in the direction of x as shown in Fig. 3.

¹Model: KPX100AR.16. Radius of Curvature: 77.52 mm. Diameter: 25.4 mm. Center Thickness: 4.047 mm.

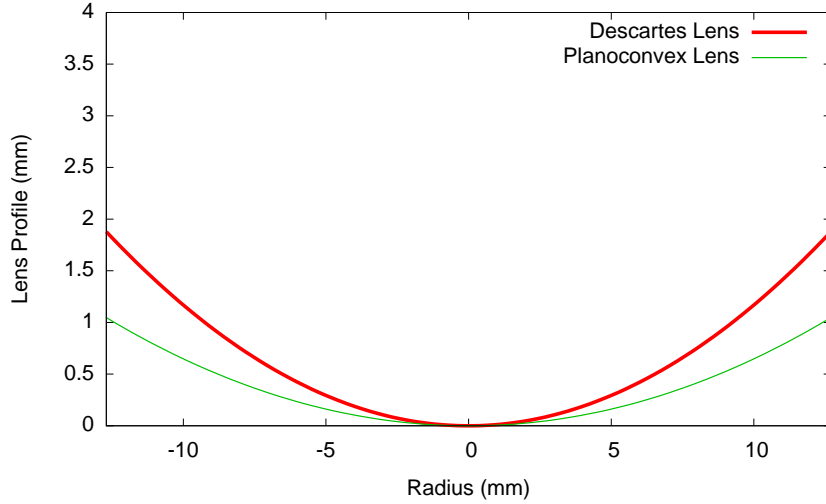


FIGURE 3. The profile of Descartes’ perfect lens and an off-the-shelf plano-convex lens.

The program predicts an RMS image size of zero to within machine precision. For the Newport lens the program predicts an RMS image size of 1.28×10^{-4} mm.

Wolf Lens

A paper by (Wolf, 1948) provides a method for designing an aspheric surface as an element of an existing optical setup. He provides Fig. 4. and Eq. (2.14) for use when the aspheric lens is being designed to collimate light and is the final element of the setup.

$$x + iy = \frac{ne^{i\omega}}{n' \cos \omega - n} \int_0^h \sin \omega dh + ih \quad (2.14)$$

Then we recast Fig. 4. to match our setup; this is shown in Fig. 5., distance a from the trapped atom to the edge of the cell wall, the thickness t of the cell wall, and the asphere’s center thickness D .

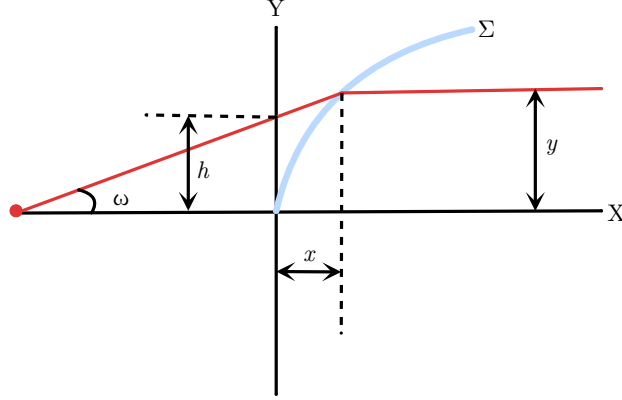


FIGURE 4. Recreated from (Wolf, 1948), for use in deriving aspheric surfaces.

First we relate the angles θ and ω via Snell's Law: $n_v \sin(\theta) = n_g \sin(\omega)$. Then we define the function $h(\omega)$,

$$h(\omega) = a \tan(\theta) + (t + D) \tan(\omega) = \frac{an_g \sin(\omega)}{\sqrt{n_v^2 - n_g^2 \sin^2(\omega)}} + (t + D) \tan(\omega). \quad (2.15)$$

To compute the integral in Eq. (2.14) we first must change the differential from dh to $d\omega$ via $dh = (\partial h(\omega)/\partial \omega)d\omega$ and compute the partial derivative,

$$\frac{\partial h(\omega)}{\partial \omega} = \frac{an_g n_v^2 \cos(\omega)}{(n_v^2 - n_g^2 \sin^2(\omega))^{3/2}} + (t + D) \sec^2(\omega). \quad (2.16)$$

The limits of the integral change from $[0, h]$ to $[0, \omega']$. Now we compute the integral and find:

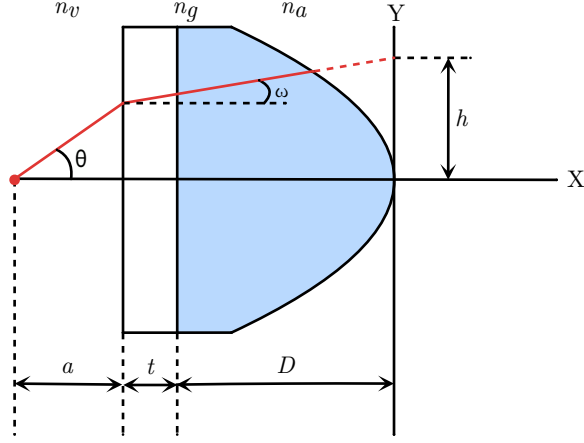


FIGURE 5. Diagram for the derivation of the “ideal collimating” asphere for our setup.

$$\begin{aligned}
 x + iy = \frac{n_g e^{i\omega}}{n_a \cos \omega - n_g} & \left((t + D) \sec(\omega) + \frac{an_v^2 \sqrt{2}}{n_g \sqrt{n_v^2 - n_g^2 \sin^2(\omega)}} - \left(t + D + \frac{a}{n_g} \right) \right) \\
 & + i \left(\frac{an_g \sin(\omega)}{\sqrt{n_v^2 - n_g^2 \sin^2(\omega)}} + (t + D) \tan(\omega) \right) \quad (2.17)
 \end{aligned}$$

We take the real and imaginary parts of Eq. (2.17) to obtain parametric equations for the asphere’s profile, $x(\omega)$ and $y(\omega)$, shown in Fig. 6. The constants a and t are fixed by our system at 10 mm and 5 mm respectively. The constant D is left undetermined by this method. We fix a value for D by requiring that the edge of the lens be 5 mm thick, chosen so that the lens has a surface to grab for mounting.

The ray tracing program is set up to use a pair of these lenses, the first to collimate the light and the second to refocus it. The program predicts an RMS image size of 5.92×10^{-10} mm. The problem with this lens is that once the point

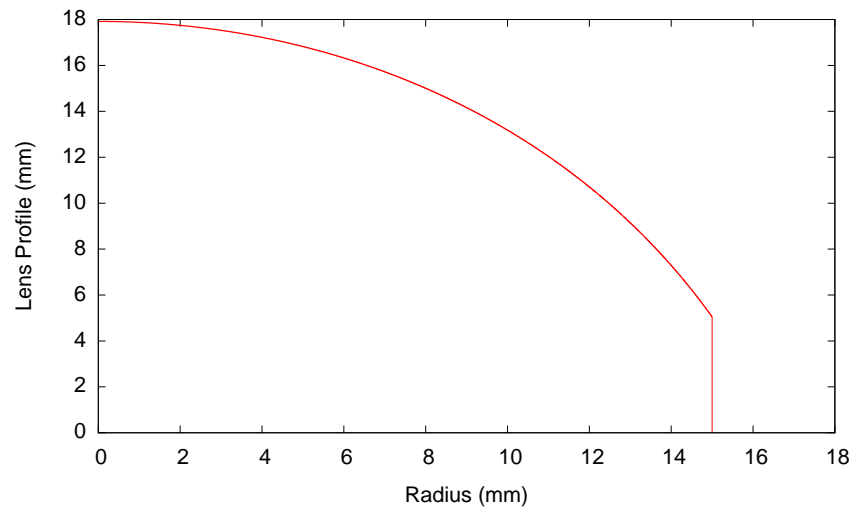


FIGURE 6. Profile of the Wolf Asphere.

source moves away from the focal point the image size increases rapidly. We have to optimize the form of the asphere to overcome this problem.

CHAPTER III

OPTIMIZATION METHODS

Gradient-Descent Optimization

Gradient-Descent Optimization attempts to search for the function's minimum using its gradient. This method requires that the objective function be convex and that its gradient be Lipschitz continuous¹ to ensure that a local minimum can be found. Code was modeled on the method shown in Fig. 7.

-
- Choose an initial point \vec{x} .
 - Repeat until termination:
 - * Calculate a new position according to: $x \leftarrow x - \gamma \nabla f(x)$ for a variety of values of γ , choosing the value of x such that $f(x)$ is minimized.

FIGURE 7. Pseudocode description of the Gradient-Descent method (Zwillinger, 2003).

Testing different values of γ is referred to as conducting a “line search”, and as implemented the code tests ten values. There are large values for γ , $\{10, 1, .1\}$, to make fast initial progress, and small values, $\{10^{-17}, \dots, 10^{-10}\}$, to ensure that once the method nears the minimum, it does not overshoot. Using more values for γ causes each iteration to take longer, but using too few values can cause the method to calculate far more iterations than necessary.

¹Lipschitz continuity is a strong form of uniform continuity. Given a function $f : X \rightarrow Y$, and a metric, d , for each space, then f is Lipschitz continuous if for all $x_1, x_2 \in X$ there exists a $K \geq 0$ such that $d_Y(f(x_1), f(x_2)) \leq K d_X(x_1, x_2)$.

While the method can guarantee success if the objective function fulfills the previously listed requirements, it can require a large number of steps. Every iteration of the algorithm requires that the gradient be calculated, which can become very computationally expensive as the dimensionality of the system increases.

Nelder-Mead Algorithm

The Nelder-Mead is a heuristic² optimization algorithm that performs a direct search of the parameter space to find a minimum. Code was modeled on the method shown in Fig. 8. The method uses the idea of an $N + 1$ dimensional simplex³ moving through an N dimensional parameter space in such a way that one of the vertices finds a minimum value for the function. It compares the function's value at every vertex, attempting to replace the vertex with the largest function value. Figure 9. shows a two-dimensional example of the different simplexes that the method generates.

The method depends on four constant parameters: ρ , χ , γ , σ . The typical values of these parameters are summarized in Table 1., and were taken from (Wright, 1996).

There are drawbacks to this method, as a heuristic it makes no demands on the function it attempts to minimize, and as a result, the method cannot guarantee success. Also it can, under certain circumstances, converge to non-stationary points (McKinnon, 1996).

²Also known as derivative-free or direct-search methods, heuristic optimization methods make no assumptions about the objective function's continuity, differentiability, or any other property.

³Simplexes generalize the idea of a triangle to arbitrary dimensions. For example, a 2-simplex is a triangle and a 3-simplex is a tetrahedron.

-
- For an N dimensional function, choose $N + 1$ initial points.
 - Sort: Label the initial points \vec{x}_i such that: $f(\vec{x}_1) \leq \dots \leq f(\vec{x}_{N+1})$.
 - Until termination repeat:
 1. Compute: $\vec{x}_0 = \sum_{i=1}^N \frac{\vec{x}_i}{N}$.
 2. Reflection: Compute $\vec{x}_r = \vec{x}_0 + \rho(\vec{x}_0 - \vec{x}_{N+1})$.
 - * If $f(\vec{x}_1) \leq f(\vec{x}_r) < f(\vec{x}_N)$ then $\vec{x}_{N+1} \leftarrow \vec{x}_r$, and return to Sort.
 - * Else continue to step 3.
 3. Expansion: If $f(\vec{x}_r) < f(\vec{x}_1)$ then compute $\vec{x}_e = \vec{x}_0 + \chi(\vec{x}_0 - \vec{x}_{N+1})$. Else continue to step 4.
 - * If $f(\vec{x}_e) < f(\vec{x}_r)$ then $\vec{x}_{N+1} \leftarrow \vec{x}_e$. Return to Sort.
 - * Else if $f(\vec{x}_e) \geq f(\vec{x}_r)$ then $\vec{x}_{N+1} \leftarrow \vec{x}_r$. Return to Sort.
 4. Contraction: If $f(\vec{x}_N) \leq f(\vec{x}_r) < f(\vec{x}_{N+1})$ then compute: $\vec{x}_c = \vec{x}_0 + \gamma(\vec{x}_r - \vec{x}_0)$. Else continue to step 5.
 - * If $f(\vec{x}_c) \leq f(\vec{x}_r)$ then $\vec{x}_{N+1} \leftarrow \vec{x}_c$. Return to Sort.
 5. Reduction: $\vec{x}_i \leftarrow \vec{x}_1 + \sigma(\vec{x}_i - \vec{x}_1)$ for $i \in \{2 \dots N + 1\}$. Return to Sort.
-

FIGURE 8. Pseudocode description of the Nelder-Mead method (Wright, 1996).

Particle-Swarm Optimization

Particle-Swarm Optimization is a direct search method that relies on the idea of swarm intelligence to minimize a function. Code was modeled on the method shown in Fig. 10. To begin, several “particles” are distributed randomly throughout the parameter space with random velocities. After every subsequent step each particle’s velocity is updated with three objectives in mind: an inertial factor causing the particle to continue in its present direction, an attraction to the point in parameter space with the best function value seen by this particular

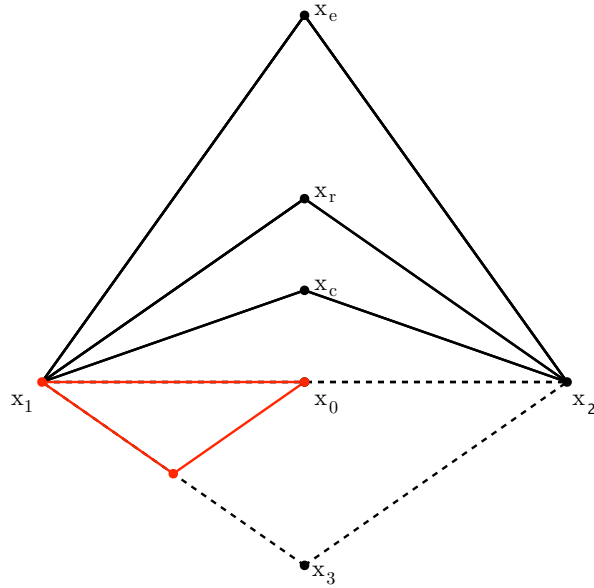


FIGURE 9. Two-dimensional example simplexes from the Nelder-Mead method.

Parameter	Value
ρ	1
χ	2
γ	$\frac{1}{2}$
σ	$-\frac{1}{2}$

TABLE 1. Suggested values for Nelder-Mead parameters.

particle, and an attraction to the point in parameter space with the best function value that the entire swarm has ever detected.

There are four parameters in this method that must be set by the user in advance: N, ω, ϕ_p , and ϕ_g . The number of particles is given by N . The remaining three parameters determine the weights of different factors in the velocity update formula: the inertial factor ω , the individual particle weight ϕ_p , and the global swarm weight ϕ_g . Several papers (Pedersen, 2009; de Weck, 2004) have suggested ranges for each parameter, shown in Table 2. One reference (Pedersen, 2010) actually provides tables suggesting specific parameter values based on both the

-
- Initialize N particles with random velocities and positions (within some user-defined bounds appropriate for the given problem).
 - Until termination, repeat for all N particles:
 - * Initialize the random variables: $r_p, r_g \sim U(0, 1)$.
 - * Update the particle’s velocity according to:

$$\vec{v} \leftarrow \omega \vec{v} + \phi_p r_p (\vec{p} - \vec{x}) + \phi_g r_g (\vec{g} - \vec{x}).$$
 - * Update the particles position: $\vec{x} \leftarrow \vec{x} + \vec{v} dt$.
 - * If $f(\vec{x}) < f(\vec{p})$ then update this particle’s best known location: $\vec{p} \leftarrow \vec{x}$.
 - * If $f(\vec{x}) < f(\vec{g})$ then update the swarm’s best known location: $\vec{g} \leftarrow \vec{x}$.
-

FIGURE 10. Pseudocode description of the Particle-Swarm Optimization method (Pedersen, 2009).

system’s dimensionality and an approximate number of function calls desired or expected. As with the Nelder-Mead algorithm, because this is a heuristic method,

Parameter	(Pedersen, 2009)	(de Weck, 2004)
N	[1,200]	No Suggestion
ω	[-2,2]	[0.4,1.4]
ϕ_p	[-4,4]	[1.5,2]
ϕ_g	[-4,4]	[2,2.5]

TABLE 2. Suggested ranges for Particle-Swarm parameters.

no guarantees can be made about its ability to discover local or global minima.

Method Comparison

The Rosenbrock function,

$$R(x, y) = (1 - x)^2 + 100(y - x^2)^2, \tag{3.1}$$

is widely used as a performance test for minimization methods. Figure 11. shows

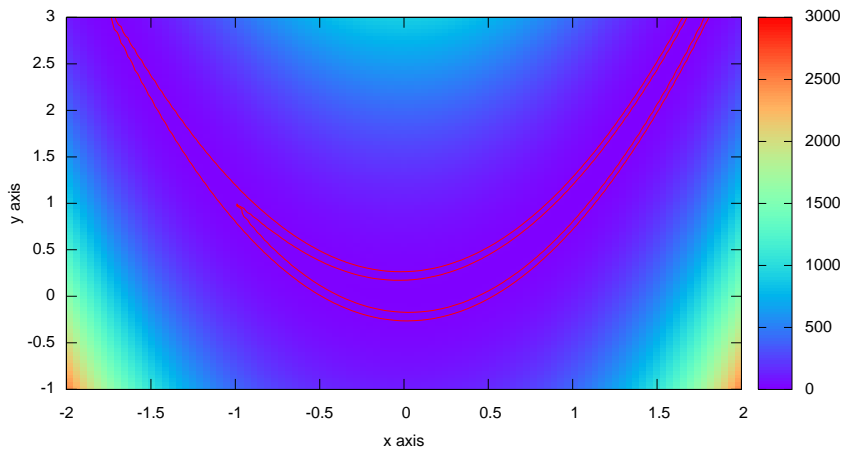


FIGURE 11. The Rosenbrock function.

a colormap of the Rosenbrock function over the relevant ranges. It is a strong candidate for testing as it has a single global minimum of zero at $(1, 1)$, it is neither convex nor is its derivative (globally) Lipschitz, and there are regions of large and small gradients.

Gradient-Descent was started at $(-1, 1)$, Nelder-Mead began with vertices at $(-1, 1)$, $(0, 2.8)$, $(-1.5, 2.6)$, and Particle-Swarm started with 17 particles randomly distributed (though it received no advantage herein; the swarm's best position at initialization was worse than where Gradient-Descent method started). Finding a function value smaller than 5×10^{-13} is the termination condition for all methods.

One of the main differentiating features among these optimization methods is how many times per iteration a method computes the objective function. In the case of ray casting, every function call takes nearly a half second, so the best method will be the one that calls on the function the fewest number of times while

still finding the minimum. Table 3. shows how different factors affect the number of function calls each method makes per iteration.

Method	Number of function calls per iteration
Gradient-Descent	$2 \times \text{dim} + \text{line search}$
Nelder Mead	$[\text{dim}+2, 2 \times \text{dim}-1]$
Particle-Swarm	Number of particles

TABLE 3. Generalized number of function calls for each method per iteration.

To make a fair comparison between each method we have to plot their progress in minimization versus the number of function calls and not versus iteration number. Figure 12. is a plot of all three methods' progress attempting to minimize the Rosenbrock function, and Table 4. shows how many function calls each method made. Based on the results of this test, it appears that Particle-Swarm Optimization is the best candidate to find a solution to the asphere problem.

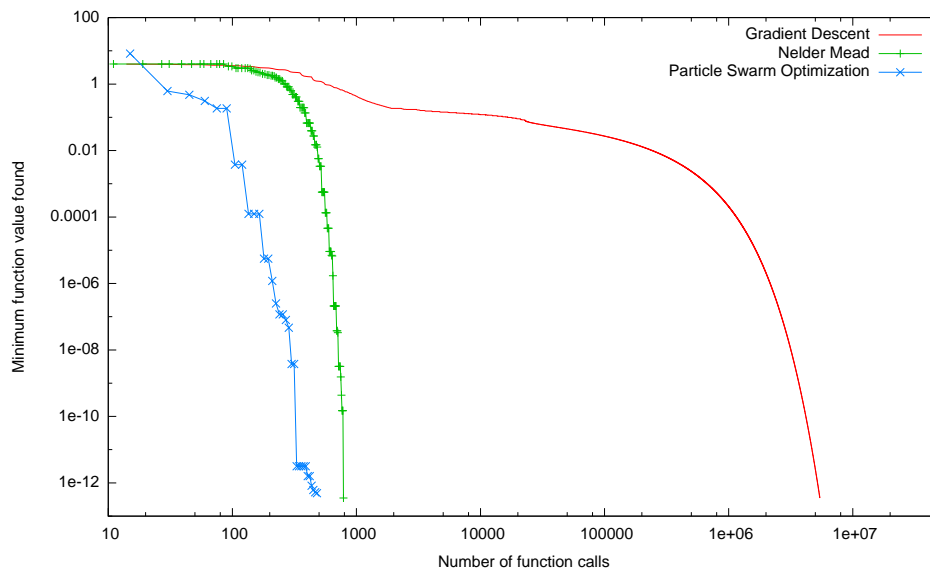


FIGURE 12. A comparison of the performance of three different optimization methods applied to the Rosenbrock function.

Method	Total Function Calls
Gradient-Descent	5433820
Nelder Mead	787
Particle-Swarm	480

TABLE 4. Total number of function calls necessary to minimize the Rosenbrock function.

CHAPTER IV

LENS DESIGN

We model the aspheric lens as a conic section with even-ordered polynomial correction terms,

$$Z(r) = \frac{Cr^2}{1 + \sqrt{1 - (1+k)C^2r^2}} + \sum_{i=0}^{10} D_{2i}r^{2i}. \quad (4.1)$$

We limit the polynomial correction term to 20th order because the manufacturing methods do not take any higher order terms. Our system can be modeled as a series of five interfaces (cell wall, first asphere, second matching asphere, back of the optical flat, and finally the image plane) shown in Fig. 13. We assume that the gap between the the back of the first asphere and the front of the cell wall will be completely filled with index matching gel, and similarly with the gap between the back of the second asphere and the optical flat. Care was taken to ensure that the aspheres would be made from a material with an index of refraction that perfectly matches the index of the glass cell. Refractive-index data are given in Appendix B.

In an effort to maintain reflection symmetry, both aspheric lens have the same profile, and the second asphere has an optical flat behind it to match the thickness of the cell wall. Additionally, the distance from the image plane to the back of the optical flat is the same as the distance from the trapped atom is from the edge of the cell wall.

There are 13 free parameters in the asphere's profile (C , k , and the 11 D_i 's), and another free parameter in the distance between the two aspheres, all



FIGURE 13. Scale representation of the imaging system.

other distances being fixed. The problem then is to determine the combination of parameters that minimizes the image size over a wide range of emitter positions.

Every calculation tests 11 emitter positions evenly distributed along a stretch of 0.5 mm. The full calculation then averages every image size. Figure 14. shows an example of the different transverse positions of the emitter. We do not test the lens with the point source at different vertical positions because the atom is well confined by the dipole trap in that direction.

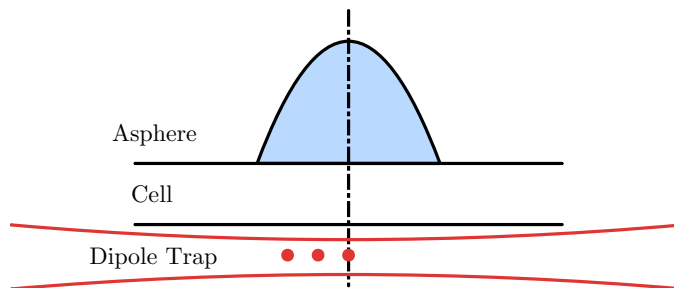


FIGURE 14. Example of different emitter positions (shown as red spots).

We use Particle-Swarm Optimization to find a solution. At the outset of the program one particle is initialized to the Wolf lens profile, and the rest are distributed randomly about that point in parameter space. Figure 15. shows the average spot size versus the iteration number. The optimization was allowed to run

for 6200 steps, though after step 320 no better average spot size was found. The final average image size found was 5.84 microns.

For the sake of completeness both Gradient-Descent optimization and the Nelder-Mead method were also used in an attempt to find a better solution; they were unable to do so.

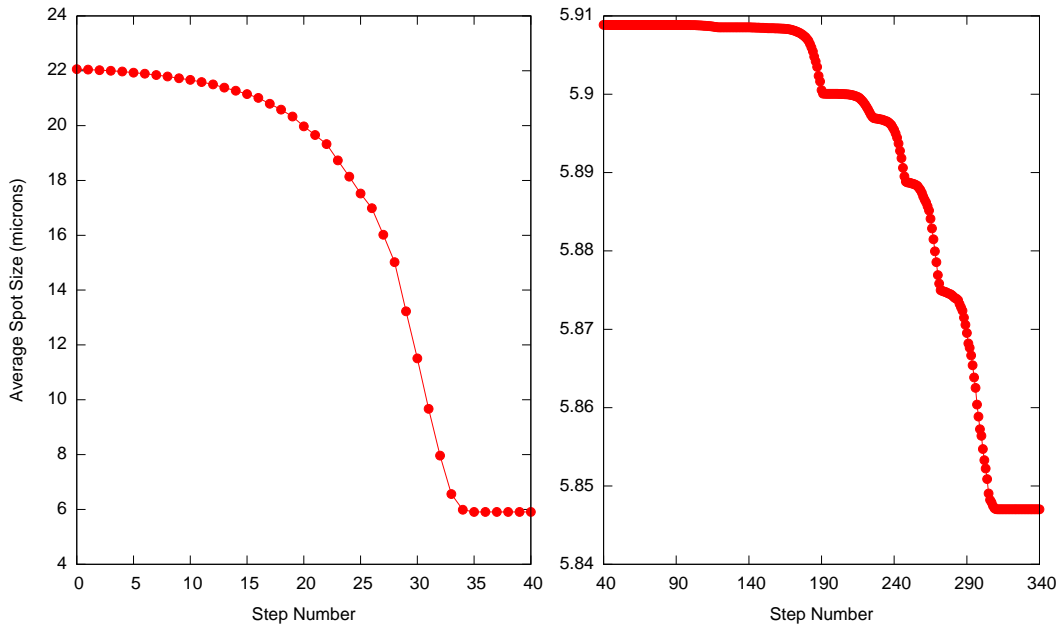


FIGURE 15. Optimization of the asphere problem.

Offset Position (mm)	0	0.05	0.1	0.15	0.2	0.25	0.3	0.35	0.4	0.45	0.5
RMS Image Size (microns)	5.27	5.06	4.43	3.38	1.91	0.38	2.39	5.14	8.33	11.9	16.0

TABLE 5. Image size as a function of emitter position for the optimized asphere.

To ensure that the lens system does not depend too sensitively on its alignment or the form of the aspheres we ran numerical simulations of the its robustness. A five micron shift in either asphere's center thickness causes a 19%

increase in the average spot size. To ensure that neither asphere is “too thick”, we ordered them short, reducing the thickness by 0.15 mm, intending to make it up with index-matching fluid. No other aspect of the setup is as sensitive.

CHAPTER V

RESULTS

The lenses were ordered from Optimax Systems, Inc. They were able to produce the aspheres to within a profile tolerance of five microns. The lens can be seen in Fig. 16.

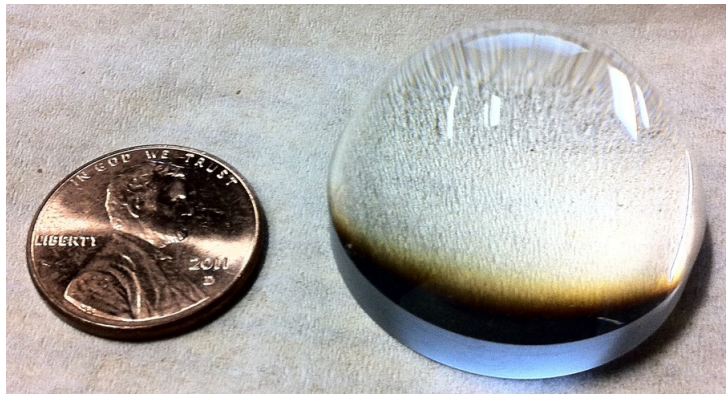


FIGURE 16. Photo of one of the 30mm diameter custom aspheric lens with a penny for comparison.

Custom parts were made in the machine shop to hold the aspheres. The first set, shown in Fig. 17., allow for the distance between the second asphere and the optical flat to be finely adjusted. They are shown mounted to the Hamamatsu C9100, which has square pixels 16 microns to a side. Another set of parts were made to hold the asphere against the glass cell, shown in Fig. 18. Machine drawings for these parts are available in Appendix C.

For testing we simulate the setup shown in Fig. 13. by substituting the cell by an optical flat. Several pictures were taken to align and characterize the system. To get the system initially aligned we first imaged a ruler etched on a glass plate, shown in Fig. 19. and then we imaged a square reticle, shown in Fig. 20.

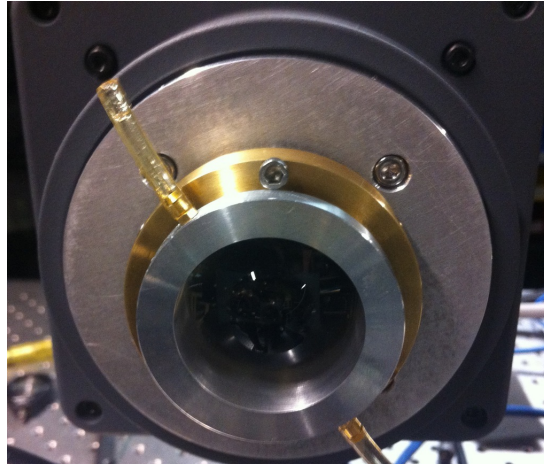


FIGURE 17. Machined parts for holding the second asphere and optical flat, pictured mounted to the Hamamatsu camera.

As a final test we imaged a bare single-mode fiber. The fiber was mounted to our Soloist air-bearing translation stage which has position resolution of 5 nm and a repeatability of 0.1 microns. The fiber has a core diameter of 5 microns (compared to the camera's 16 micron square pixels), and was moved over a range of 0.5 mm from the center of the lenses outward. Pictures were taken at ten micron intervals.

Figure 21. shows the image of the fiber at the center position. The most illuminated pixel contains 42% of the total intensity, its illuminated neighboring pixels contain approximately 8% each. As the fiber is moved out to the edge of the optimized range, 0.5 mm away from the central axis, the spot size increases only marginally as shown in Fig. 22.

Shown in Fig. 23. are a series of 11 images, the first taken 0.1 mm away from the center of the lens with each successive image taken ten microns farther out. The vertical displacement is done only for clarity, the spot stayed in the same two rows of pixels. Based on the movement of the brightest pixel it is clear that

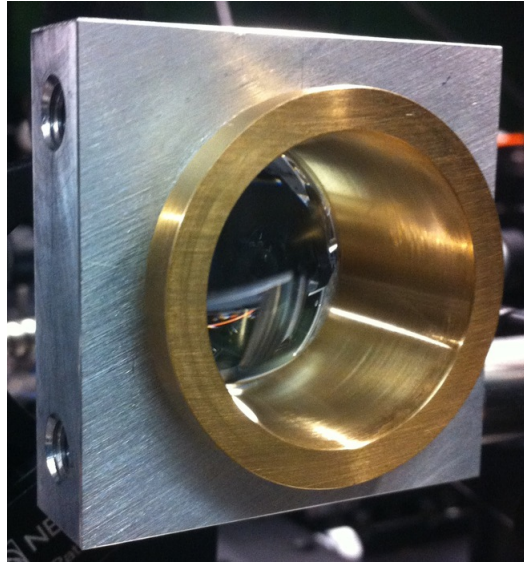


FIGURE 18. Machined parts for mounting the first asphere to the glass cell.

the imaging system has at minimum the ability to distinguish the position of an emitter to within ten microns.

For comparison we imaged the same fiber with a pair of 1 inch diameter, 25.4 mm focal length lenses separated by 90 mm, the same separation as the aspheres. Again, pictures were taken with the Hamamatsu camera. Figures 24. and 25. show the image at the center of the imaging system and 0.5 mm off-axis. For comparison, Fig. 26. shows the spot size for the aspheric imaging system when the fiber is 1.5 mm off-axis, well outside the range for which the system was optimized. The aspheric imaging system produces a more localized spot, exactly what the system was designed to do.

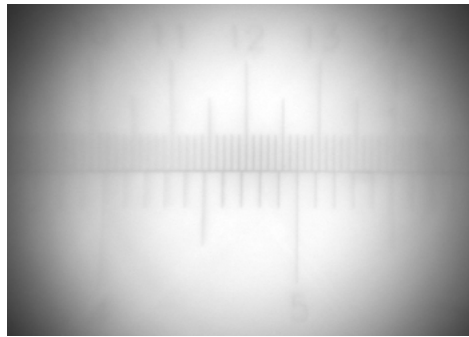


FIGURE 19. Image of an etched ruler taken with the aspheres. Measurements on top are in millimeters.

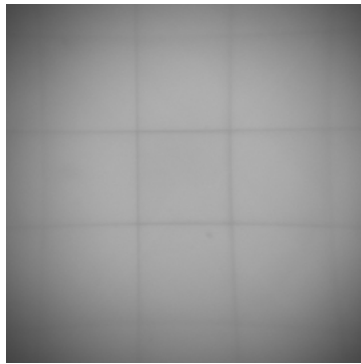


FIGURE 20. Image of a square reticle showing slight pincushion distortion.

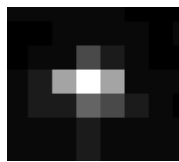


FIGURE 21. Image of a single-mode optical fiber at the center of the aspheric imaging system.



FIGURE 22. Image of a single-mode optical fiber 0.5 mm away from the center of the aspheric imaging system.

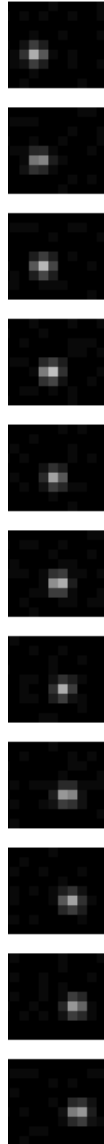


FIGURE 23. A series of images as the optical fiber is shifted away from the central axis of the aspheric imaging system.

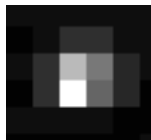


FIGURE 24. Image of a single-mode optical fiber at the center of the plano-convex imaging system.



FIGURE 25. Image of a single-mode optical fiber 0.5 mm away from the center of the plano-convex imaging system.



FIGURE 26. Image of a single-mode optical fiber approximately 1.5 mm away from the center of the aspheric imaging system.

CHAPTER VI

CONCLUSIONS

We have provided a general method for designing an imaging system given almost any existing or desired system geometry. Using this method we designed a pair of aspheric lenses to image a point source to a point independent of the emitter's position. Additionally, the lenses were designed to have a very large numerical aperture, making them a feasible imaging system for monitoring the position of a single atom. We tested the lens system and found that it performed as well as predicted, and that it out performed a similar system built with conventional lenses.

APPENDIX A

SNELL'S LAW

We prove here that \hat{v}_{refract} is a unit vector provided that \hat{N} and \hat{L} are also unit vectors. The relevant equations are:

$$\cos(\theta_1) = \hat{N} \cdot (-\hat{L}), \tag{A.1}$$

$$\cos(\theta_2) = \sqrt{1 - \left(\frac{n_1}{n_2}\right)^2 (1 - (\cos(\theta_1))^2)}, \tag{A.2}$$

$$\hat{v}_{\text{refract}} = \left(\frac{n_1}{n_2}\right) \hat{L} + \left(\frac{n_1}{n_2} \cos(\theta_1) - \cos(\theta_2)\right) \hat{N}. \tag{A.3}$$

We begin by taking the inner product of \hat{v}_{refract} with itself, using the form given in Eq. (A.3), and find,

$$\begin{aligned} |\hat{v}_{\text{refract}}|^2 &= \hat{v}_{\text{refract}} \cdot \hat{v}_{\text{refract}}, \\ |\hat{v}_{\text{refract}}|^2 &= \left(\frac{n_1}{n_2}\right)^2 \hat{L} \cdot \hat{L} + 2 \left(\frac{n_1}{n_2}\right) \left(\frac{n_1}{n_2} \cos(\theta_1) - \cos(\theta_2)\right) \hat{L} \cdot \hat{N} \\ &\quad + \left(\frac{n_1}{n_2} \cos(\theta_1) - \cos(\theta_2)\right)^2 \hat{N} \cdot \hat{N}. \end{aligned}$$

Now we substitute with Eq. (A.1),

$$\begin{aligned}
|\hat{v}_{\text{refract}}|^2 &= \left(\frac{n_1}{n_2}\right)^2 + 2 \left(\left(\frac{n_1}{n_2}\right)^2 \cos(\theta_1) - \left(\frac{n_1}{n_2}\right) \cos(\theta_2) \right) (-\cos(\theta_1)) \\
&\quad + \left(\frac{n_1}{n_2} \cos(\theta_1)\right)^2 - 2 \frac{n_1}{n_2} \cos(\theta_1) \cos(\theta_2) + \cos^2(\theta_2) \\
&= \left(\frac{n_1}{n_2}\right)^2 - 2 \left(\frac{n_1}{n_2}\right)^2 \cos^2(\theta_1) + 2 \left(\frac{n_1}{n_2}\right) \cos(\theta_2) \cos(\theta_1), \\
&\quad + \left(\frac{n_1}{n_2} \cos(\theta_1)\right)^2 - 2 \left(\frac{n_1}{n_2}\right) \cos(\theta_1) \cos(\theta_2) + \cos^2(\theta_2).
\end{aligned}$$

After canceling terms we are left with,

$$|\hat{v}_{\text{refract}}|^2 = \left(\frac{n_1}{n_2}\right)^2 - \left(\frac{n_1}{n_2}\right)^2 \cos^2(\theta_1) + \cos^2(\theta_2).$$

Substituting with Eq. (A.2), we are left with,

$$\begin{aligned}
|\hat{v}_{\text{refract}}|^2 &= \left(\frac{n_1}{n_2}\right)^2 - \left(\frac{n_1}{n_2}\right)^2 \cos^2(\theta_1) + \left(1 - \left(\frac{n_1}{n_2}\right)^2 (1 - (\cos(\theta_1))^2)\right), \\
&= 1.
\end{aligned}$$

APPENDIX B

INDEX OF REFRACTION DATA

The glass cell provided by Hellma is made from a material called Spectrosil 2000. Because this material was unavailable to Optimax Systems, we had to ensure that standard fused silica would be an acceptable replacement. Data taken from (Malitson, 1965) and (Heraeus, 2011) confirm that fused silica and Spectrosil 2000 have the same index of refraction for light at 780 nm. Each paper quotes values for the six constants in Sellmeier equation,

$$n(\lambda) = \sqrt{1 + \frac{B_1\lambda^2}{\lambda^2 - C_1} + \frac{B_2\lambda^2}{\lambda^2 - C_2} + \frac{B_3\lambda^2}{\lambda^2 - C_3}} \quad (\text{B.1})$$

summarized in Table 6.

	Spectrosil 2000	Fused Silica
B_1	4.73115591×10^1	6.961663×10^1
B_2	6.31038719×10^1	4.079426×10^1
B_3	9.06404498×10^1	8.974794×10^1
C_1	$1.29957170 \times 10^{-2}$	4.679148×10^{-2}
C_2	$4.12809220 \times 10^{-3}$	1.351206×10^{-2}
C_3	9.87685322×10^1	9.793400×10^1
Source	(Heraeus, 2011)	(Malitson, 1965)

TABLE 6. Sellmeier constants for Spectrosil 2000 and fused silica.

At 780 nm the index of refraction between these two materials differs by 4.7×10^{-6} (with a value of 1.453675), which is less than the error stated in (Malitson, 1965).

To bridge the gap between the lenses and either the cell wall or optical flat, we bought two index matching fluids and one index matching gel. These materials

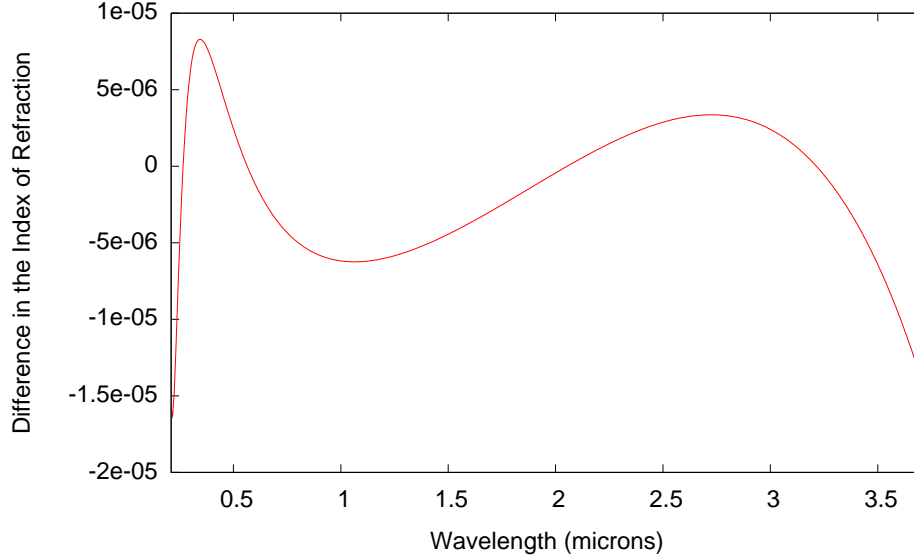


FIGURE 27. Difference in the index of refraction for Spectrosil 2000 and fused silica.

were purchased from Cargille Labs. They provide values for use with the Cauchy equation,

$$n(\lambda) = W_1 + W_2/\lambda^2 + W_3/\lambda^4, \quad (\text{B.2})$$

to determine each materials index of refraction for any wavelength. Values for each material are summarized in Table 7. and were taken from each materials characteristics sheet, provided by Cargille Labs.

Constant	Fluid #50350	Fluid #06350	Gel #0608
W_1	1.446902	1.447193	1.44514
W_2	398962.9	383343.3	431760
W_3	3.757747×10^{11}	5.661342×10^{11}	-1.80659×10^{11}

TABLE 7. Cauchy constants for the index matching materials.

Table 8. shows the index of refraction for each material. Fluid #06350 gives the best match though it is nearly as viscous as water, meaning that it would be a

real challenge to use. Gel #0608 is very easy to work with but provides the worst index matching of the three. All data shown in this thesis was taken with the index matching gel.

	Fluid #50350	Fluid #06350	Gel #0608
Index of Refraction	1.45356	1.45364	1.45218

TABLE 8. The index of refraction of all three index matching materials at 780 nm.

APPENDIX C

MECHANICAL DRAWINGS

We designed custom hardware to mount the aspheres to our system. Figure 28. shows the two piece system that will mount the first asphere to the cell wall. All dimensions are shown in millimeters. A picture of these parts can be seen in Fig. 18.

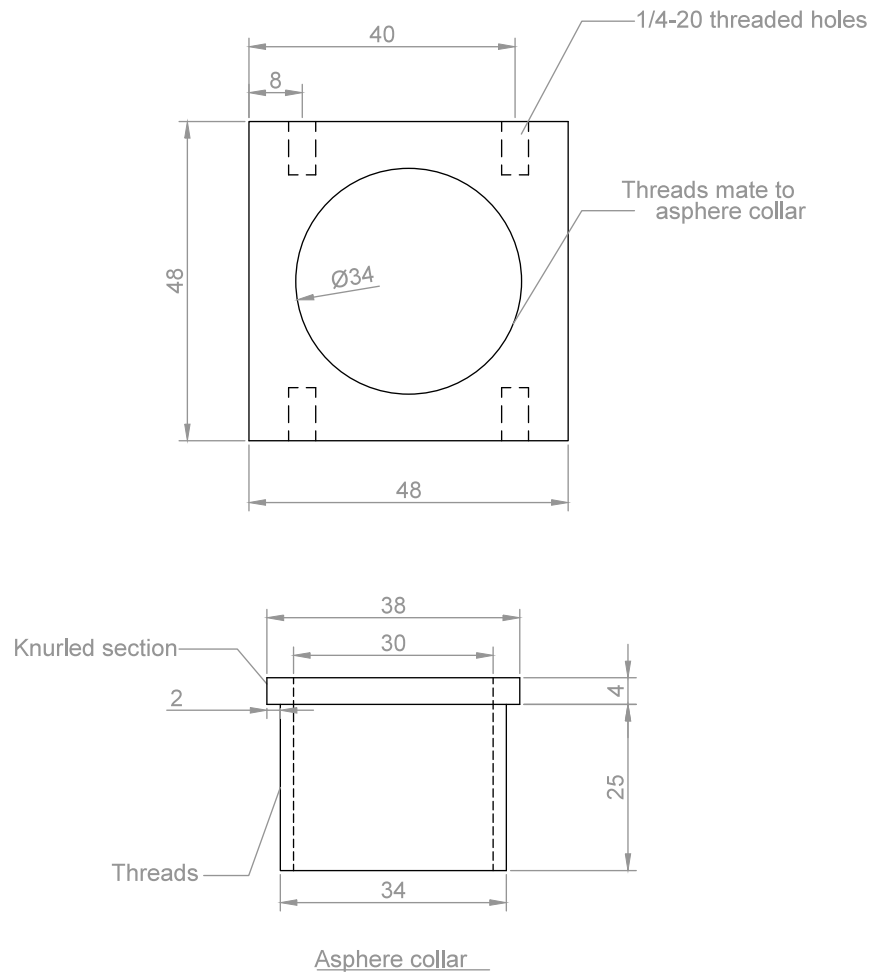


FIGURE 28. Mechanical drawing of the asphere collar and mounting piece.

For mounting the asphere and the glass plate to the Hamamatsu camera we designed a new front plate with a wider opening, shown in Fig. 29. Detailed drawings of the asphere collar and glass plate holder are shown in Fig. 30. All three parts are shown assembled and attached to the camera in Fig. 17. To prevent the threads from binding the glass plate holder was machined from brass. Each threaded piece has a pitch of 40 threads-per-inch, allowing for very fine adjustment of the optics. A port in the asphere collar allows index-matching fluid to be injected, filling the gap between the asphere and the glass plate.

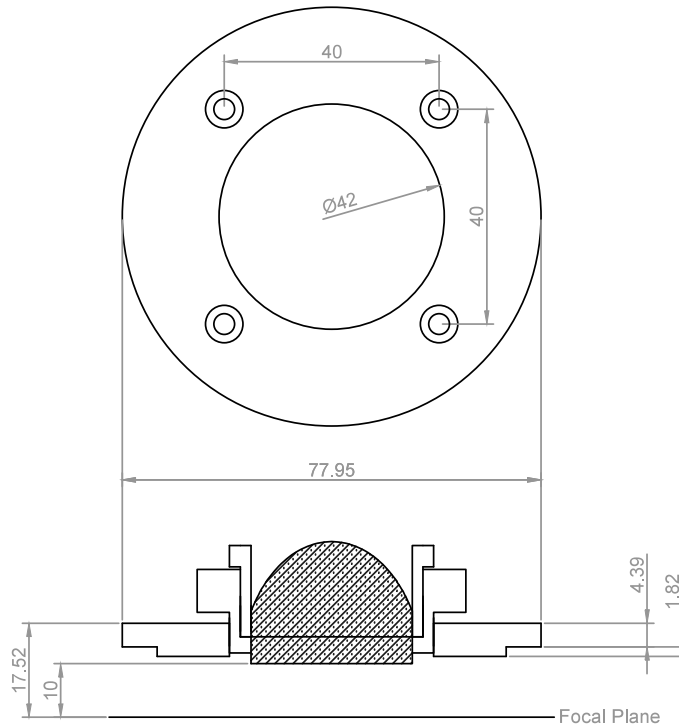


FIGURE 29. Mechanical drawing of the asphere mounting parts for the Hamamatsu camera.

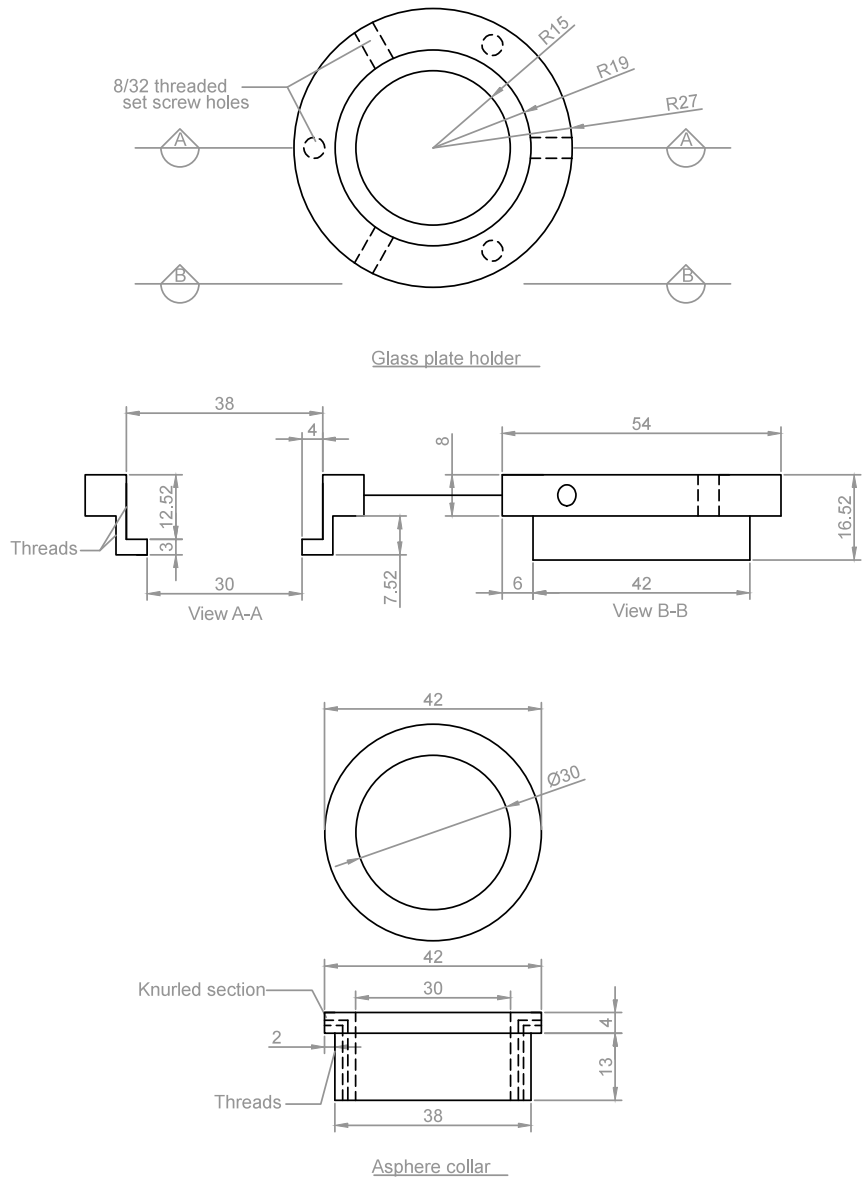


FIGURE 30. Detail drawings of the glass plate holder and the asphere collar.

APPENDIX D

ASPHERE PROFILE

To reiterate, the asphere equation is given by,

$$Z(r) = \frac{Cr^2}{1 + \sqrt{1 - (1+k)C^2r^2}} + \sum_{i=0}^{10} D_{2i}r^{2i}. \quad (\text{D.1})$$

The optimization program used every parameter to determine the best aspheric profile, however Optimax systems charges for every coefficient beyond D_4 . Because of this we fit an asphere equation truncated to fourth order to the best profile found through optimization. We were able to do this with a residual less than the form error Optimax advertises. Table 9. shows the final values submitted to Optimax (for use with Eq. (D.1) when r is in millimeters).

Constant	Value
C	-0.128
k	-0.824
D_0	17.705
D_2	2.11×10^{-2}
D_4	8.71×10^{-2}

TABLE 9. Final values for the parameters of the asphere equation.

REFERENCES CITED

- Alt, W. (2008). An objective lens for efficient fluorescence detection of single atoms. *International Journal for Light and Electron Optics*.
- Blinov, B. B. (2009). Trapped ion imaging with a high numerical aperture spherical mirror. *Journal of Physics B: Atomic, Molecular and Optical Physics*, 42.
- de Weck, O. (2004). *A comparison of particle swarm optimization and the genetic algorithm* (Tech. Rep.). American Institute of Aeronautics and Astronautics.
- Glassner, A. S. (1989). *An introduction to ray tracing*. Morgan Kaufmann.
- Heraeus. (2011). *Quartz glass for optics data and properties* (Tech. Rep.). Heraeus Quartz America.
- J.A. Nelder, R. M. (1965). A simplex method for function minimization. *The Computer Journal*, 7, 308-313.
- Kingslake, R. (2010). *Lens design fundamentals* (Second ed.). Elsevier.
- Malitson, I. H. (1965). Interspecimen comparison of the refractive index of fused silica. *Journal of the Optical Society of America*, 55(10), 1205-1209.
- McKinnon, K. (1996, May). Convergence of the nelder-mead simplex method to a non-stationary point. *SIAM Journal on Optimization*.
- Pedersen, M. E. H. (2009). Simplifying particle swarm optimization. *Applied Soft Computing*.
- Pedersen, M. E. H. (2010). *Good parameters for particle swarm optimization* (Tech. Rep.). <http://www.hvass-labs.org/people/magnus/publications/pedersen10good-pso.pdf>: Hvass Laboratories.
- Wolf, E. (1948). On the designing of aspheric surfaces. *Proceedings of the Physical Society*, 61(6).
- Wright, P. E. (1996, November). Convergence properties of the nelder-mead simplex method in low dimensions. *SIAM Journal on Optimization*, 9(1), 112-147.
- Zwillinger, D. (Ed.). (2003). *Crc standard mathematical tables and formulae* (31st ed.). Chapman & Hall/CRC.